Biogeosciences

The role of alkalinity generation in controlling the fluxes of CO_2 during exposure and inundation on tidal flats

P. A. Faber[1], A. J. Kessler[1], J. K. Bull[1], I. D. McKelvie[2,3], F. J. R. Meysman[4], and P. L. M. Cook[1]

[1]Water Studies Centre, School of Chemistry, Monash University, Victoria 3800, Australia
[2]School of Chemistry, The University of Melbourne, Victoria 3010, Australia
[3]School of Geography, Earth and Environmental Sciences, University of Plymouth, Plymouth PL48AA, UK
[4]Department of Ecosystem Studies, Royal Netherlands Institute for Sea Research (NIOZ), Korringaweg 7, 4401 NT Yerseke, The Netherlands

Correspondence to: P. A. Faber (peter.faber@monash.edu)

Abstract. Dissolved inorganic carbon (DIC), gaseous CO_2 and alkalinity fluxes from intertidal sediments were investigated during periods of exposure and inundation, using laboratory core incubations, previously published field data and reactive transport model simulations. In the incubations and previous field data, it was found that during periods of alkalinity production (attributed to the accumulation of reduced sulfur species within the sediment), the flux of DIC out of the sediment was greater during inundation than the gaseous CO_2 flux during exposure by a factor of up to 1.8. This finding was supported by computational simulations which indicated that large amounts of sulfate reduction and reduced sulfur burial (FeS) induce an alkalinity flux from the sediment during high tide conditions. Model simulations also found that the amount of reactive Fe in the sediment was a major driver of net alkalinity production. Our finding that CO_2 fluxes can be significantly lower than total metabolism during exposure has implications for how total metabolism is quantified on tidal flats.

1 Introduction

Tidal flats are highly dynamic and biogeochemically active environments, that are characterised by the deposition of allochthonous organic matter as well as high in situ rates of primary production by microphytobenthos (Joye et al., 2009). The quantification of organic carbon production and mineralisation in these environments is compli-
cated by the fact that tidal flats are periodically inundated. This means that fluxes of inorganic carbon should ideally be measured both during inundation (as dissolved inorganic carbon DIC = $[CO_2] + [HCO_3^-] + [CO_3^{2-}]$) and exposure (as gaseous CO_2). In practice, the quantification of inorganic carbon fluxes during the inundation of tidal flats is logistically complex because they are covered by a shallow layer of turbid water and often experience high currents. Moreover, the determination of DIC in aqueous samples is also more time consuming and technically challenging than the analysis of CO_2 in gas samples. Typically, most studies of benthic metabolism on tidal flats only measure gaseous fluxes of CO_2 during exposure (Migné et al., 2005; Middelburg et al., 1996) or DIC flux during inundation (Cai et al., 1999).

Relatively few studies have included direct measurement of inorganic carbon fluxes during both exposure and inundation of tidal flats and these studies show different outcomes. Alongi et al. (1999) found very similar exchange rates during both inundation and exposure. By contrast, Gribsholt and Kristensen (2003) and Cook et al. (2004) found consistently higher rates of inorganic carbon exchange during inundation on un-vegetated tidal flat sediments, where the flux during inundation increased by a factor of ~ 2. A number of possible explanations exist for these differences. Firstly, solute transport processes are very different between inundation and exposure periods. During inundation, all three forms of the carbonate system (CO_2, HCO_3^- and CO_3^{2-}) can be transported across the sediment interface, whereas during exposure, only gaseous CO_2 can diffuse into the atmosphere. Furthermore,

bio-irrigation is well known to enhance solute exchange in sediments (Kristensen, 1988). This process will cease upon exposure, and would result in a reduction of the CO_2 flux during exposure as compared to the inundated DIC flux. Secondly, alkalinity generation, caused by the burial of reduced metal sulfides and/or calcium carbonate dissolution, is often observed at high rates in shallow waters and intertidal sediments (Thomas et al., 2009; Cook et al., 2004; Ferguson et al., 2003). Alkalinity cannot escape the sediment during low tide and, therefore, will tend to accumulate near the sediment-water interface. This will lead to a shift towards increased HCO_3^- and CO_3^{2-} and decreased CO_2 and, hence, a reduced gaseous CO_2 flux during exposure.

However, there are also reasons why the CO_2 flux might be enhanced during exposure. A change in CO_2 transfer during exposure to the atmosphere may occur due to the higher diffusion of CO_2 in the atmosphere (10^{-5} compared to $10^{-9} \, \mathrm{m^2 s^{-1}}$) and the decreased thickness of the diffusive boundary layer during exposure (Brotas et al., 1990).

To date, none of these factors have been explored, experimentally or theoretically. A basic understanding of the exchange dynamics of inorganic carbon is required for the design of studies aiming to quantify the fluxes of inorganic carbon between tidal flats and the atmosphere and coastal waters. Here, we used data from controlled laboratory experiments and a numeric diagenetic model to investigate the dynamics of inorganic carbon exchange in the intertidal zone. In particular, we focus on the role of alkalinity generation by anaerobic respiration in the retardation of the CO_2 efflux during exposure relative to DIC export to the water column.

2 Materials and methods

2.1 Experimental

Muddy sediment (Grain size: 48 % 300 μm–1 mm; 8 % 200–300 μm; 39 % 100–200 μm; 5 % 62–100 μm and porosity = 0.81 ml water cm^{-3}) was collected from an intertidal flat located in the Yarra Estuary, Australia (37.833° S, 145.0229° E). The sediment was sieved (1 mm mesh) to remove macrofauna and homogenised. The total inorganic carbon content of the sediment was < 0.1 % w/w. The sediment was then placed in a shallow tray and gently stirred whilst being aerated for 1 day to oxidise reduced solutes before being packed into 8 core liners (7 cm diameter) to a depth of 5 cm. This depth layer was chosen to represent the diagenetically active depth. Figure 1 represents the experimental setup that was used. The cores had stirrer bars inserted to gently stir the water column. A peristaltic pump system transferred ambient sea water collected from Port Phillip Bay in and out of the cores (Salinity = 35, Temperature = 20 °C). The pumping regime followed a regular six hourly cycle of inundation and exposure that mimicked a semi-diurnal tide. The inlet of the tubes in the core was recessed slightly into the sediment
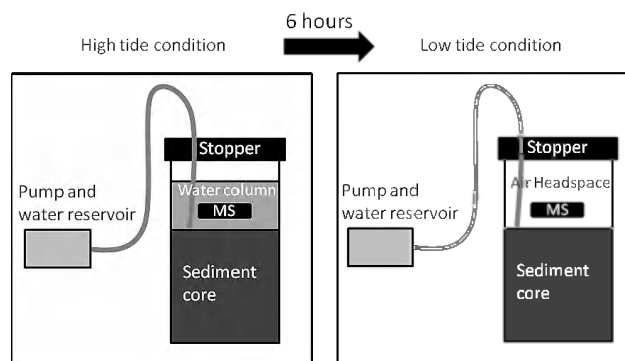

Fig. 1. Diagram of the experimental setup, showing the conditions of simulated tides. TA and DIC are sampled from the water column during inundation (high tide) and CO_2 is sampled from the headspace during exposure (low tide). MS refers to a magnetic stirrer bar.

surface, so that all the overlying water could be removed, leaving no ponding of water on the surface during exposure. Carbon mineralisation processes in natural systems can be highly dynamic reflecting pulsed inputs of organic matter (OM), for example, deposition of phytodetritus. This pulsed occurrence of carbon mineralisation is highly relevant, driving cycles of solute reduction and oxidation, which in turn drives alkalinity production and consumption. To simulate a pulse of organic matter, half of the cores had 0.38 g baker's yeast added to them after 71 days (+OM treatment), while the remaining cores did not receive this organic matter input (−OM). During inundation, the flux of DIC was determined by covering the cores with sealed lids and taking 4–5 water samples during sediment inundation. The DIC flux was determined as the slope of DIC concentration versus time multiplied by the water height. The pH was simultaneously measured as the water sample for alkalinity was taken. During exposure, the flux of gaseous CO_2 was measured by sampling the gas headspace of the sealed core. Again, the CO_2 flux was determined as the slope of CO_2 concentration versus time multiplied by the headspace height. CO_2 was sampled using evacuated 3 ml draw blood collection vials (Vacutainers, Becton Dickinson) and analysed using Flow Injection Analysis (Satienperakul et al., 2004). Alkalinity samples were filtered (Bonnet, 0.45 μm polyethersulfone) and preserved with 20 μl $HgCl_2$ (6 % w/v). They were stored in glass vials and refrigerated at 4 °C for less than one week before analysis using a modified Gran titration (Almgren et al., 1983). pH was determined at 20 °C using a pH electrode (Hach PHC301 connected to an HQ40d meter), calibrated with NBS buffers. DIC concentrations in the water column were calculated using alkalinity and pH, with the constants found in Roy et al. (1993). The method for total Fe analysis of the dried sediment was modified from Lord (1982), using a 24 h citrate/bicarbonate/dithionite extraction for easily extractable Fe, followed by a 24 h concentrated nitric acid

digestion. The extracts were then analysed using atomic absorption spectroscopy (AAS).

2.2 Model formulation

The reactive transport model follows the standard formulation for early diagenetic models of marine sediments (Boudreau, 1997; Meysman et al., 2003). The model simulates the depth profiles of solutes and solids, as well as the fluxes across the sediment-water interface, based on the mass balance equations

$$\text{Solutes: } \varphi \frac{\partial C_i^{PW}}{\partial t} = \frac{\partial}{\partial x}\left[\varphi D_i \frac{\partial C_i^{PW}}{\partial x}\right] + \sum_k v_{i,k} R_k$$

$$\text{Solids: } (1-\varphi)\frac{\partial C_i^S}{\partial t} = \sum_k v_{i,k} R_k$$

where C_i^{PW} and C_i^S are the concentrations of a solute and solid compound, respectively. No advective processes are included in the model, as negligible sedimentation occurred during the incubations. The porosity φ is assumed constant with depth. For solutes, the only transport process is molecular diffusion. The diffusion coefficient D_i is calculated as a function of temperature and salinity using the R package marelac (Soetaert et al., 2010) and subsequently corrected for tortuosity according to the modified Wiessberg relation of Boudreau (1996). The quantities R_k represent the reaction rates, where $v_{i,k}$ is the stoichiomeric coefficient of the i-th species in the k-th reaction. The reaction set includes three mineralisation pathways (aerobic respiration, dissimilatory iron reduction and sulfate reduction) for two fractions of organic matter (fast and slow decaying), the formation of iron sulfide and pyrite, and the reoxidation of reduced compounds in pore water (ferrous iron, free sulfide) and solid phase (iron sulfides and pyrite). The full set of 13 reactions is given in Table 1. The rate expressions for these reactions follow the standard kinetic rate laws and are given in Table 2. For simplicity, we have assumed that processes such as nitrification and denitrification have a negligible effect on alkalinity fluxes in this system.

2.3 pH model

The set of acid-base reactions governing the pH dynamics in the pore water includes the carbonate, borate, sulfide and water equilibria. The impact of dissociation reactions involving phosphate, ammonium, silicate and dissolved organic compounds was assumed negligible. The associated total alkalinity and total species are hence defined as:

$$A_T = \left[HCO_3^-\right] + 2\left[CO_3^{2-}\right] + \left[B(OH)_4^-\right] + \left[HS^-\right] + \left[OH^-\right] - \left[H^+\right]$$

$$\text{SumCO2} = [CO_2] + \left[HCO_3^-\right] + \left[CO_3^{2-}\right]$$

$$\text{SumBOH3} = \left[B(OH)_3\right] + \left[B(OH)_4^-\right]$$

$$\text{SumH2S} = \left[HS^-\right] + [H_2S]$$

Table 1. Kinetic reactions included in the reaction set.

R1:	$\{CH_2O\}_f + O_2 \rightarrow H_2O$
R2:	$\{CH_2O\}_f + 4\,FeOOH + 8\,H^+ \rightarrow 4\,Fe^{2+} + CO_2 + 7\,H_2O$
R3:	$\{CH_2O\}_f + \frac{1}{2}\,SO_4^{2-} + \frac{1}{2}\,H^+ \rightarrow CO_2 + \frac{1}{2}\,H^- + H_2O$
R4:	$\{CH_2O\}_s + O_2 \rightarrow CO_2 + H_2O$
R5:	$\{CH_2O\}_s + 4\,FeOOH + 8\,H^+ \rightarrow 4\,Fe^{2+} + CO_2 + 7\,H_2O$
R6:	$\{CH_2O\}_s + \frac{1}{2}\,SO_4^{2-} + \frac{1}{2}\,H^+ \rightarrow CO_2 + \frac{1}{2}\,H^- + H_2O$
R7:	$HS^- + 2\,O_2 \rightarrow SO_4^{2-} + H^+$
R8:	$Fe^{2+} + \frac{1}{4}\,O_2 + \frac{3}{2}\,H_2O \rightarrow FeOOH + 2\,H^+$
R9:	$8\,FeOOh = HS^- + 15\,H^+ \rightarrow SO_4^{2-} + 12\,H_2O$
R10:	$Fe^{2+} + HS^- \rightarrow FeS + H^+$
R11:	$FeS + \frac{9}{4}\,O_2 + \frac{3}{2}\,H_2O \rightarrow FeOOH + SO_4^{2-} + 2\,H^+$
R12:	$FeS + \frac{1}{4}\,SO_4^{2-} + \frac{3}{4}\,HS^- + \frac{5}{4}\,H^+ \rightarrow FeS_2 + H_2O$
R13:	$FeS_2 + \frac{15}{4}\,O_2 + \frac{5}{2}\,H_2O \rightarrow FeOOH + 2\,SO_4^{2-} + 4\,H^+$

The associated equilibrium constants were calculated as a function of temperature and salinity using AquaEnv, a dedicated R-package for acid-base and CO_2 system calculations (Hofmann et al., 2010).

2.4 Boundary conditions and initial state

The cyclic process of inundation and exposure was simulated by regular switching between two sets of boundary conditions. Under inundation, the concentration of solutes at the sediment-water interface was fixed to that of the overlying water (which was set at constant pH and solute concentrations), while a fixed flux was imposed for the solids. These fluxes were set to zero for all solid components during the whole simulation period (zero deposition assumed – see above), apart from organic matter, which received a pulse input at 71 days. To model this pulse input, the organic matter was added uniformly to the top 2 mm of the sediment at a total concentration of $\sim 2500\,\mu mol\,CH_2O\,g^{-1}$ dry sediment and fractionated between the fast-decaying fraction (75 %) and the slow-decaying fraction (25 %), a ratio used by Westrich and Berner (1984) (who also included a third, non-reactive fraction in their model.)

Under exposed conditions, only the volatile solutes O_2 and CO_2 have an exchange with the overlying atmosphere, which is modelled using the convective boundary flux $J = k_d\,(C^{eq} - C)$ with k_d the piston velocity and C^{eq} the gas concentration in equilibrium with the atmosphere. At the lower boundary of the sediment domain a no-flux condition was imposed (fluxes across the bottom boundary are zero) for all compounds over the whole simulation period.

The reduced Fe (FeS and FeS$_2$) concentration was initially set to 0 and the O_2 concentration in the pore water was set to equilibrium with the atmospheric concentration. A uniform profile of slow-decaying organic matter ($\sim 2500\,\mu mol\,CH_2O\,g^{-1}$ dry sediment), and either 19 or $95\,\mu mol\,Fe\,g^{-1}$ dry sediment was imposed. These latter values were determined to be the extreme low and high Fe

Table 2. Kinetic rate expressions for the reactions included in the reaction set.

$$R_{min}^{f} = (1 - \varphi) k_{fast} \left[CH_2O_f \right]$$

$$R_{min}^{s} = (1 - \varphi) k_{slow} \left[CH_2O_s \right]$$

$$R_1 = \frac{[O_2]}{[O_2] + K_{O_2}} R_{min}^{f}$$

$$R_2 = \frac{[FeOOH]}{[FeOOH] + K_{FeOOH}} \frac{K_{O_2}}{[O_2] + K_{O_2}} R_{min}^{f}$$

$$R_3 = \frac{\left[SO_4^{2-} \right]}{\left[SO_4^{2-} \right] + K_{SO_4^{2-}}} \frac{K_{FeOOH}}{[FeOOH] + K_{FeOOH}} \frac{K_{O_2}}{[O_2] + K_{O_2}} R_{min}^{f}$$

$$R_4 = \frac{[O_2]}{[O_2] + K_{O_2}} R_{min}^{s}$$

$$R_5 = \frac{[FeOOH]}{[FeOOH] + K_{FeOOH}} \frac{K_{O_2}}{[O_2] + K_{O_2}} R_{min}^{s}$$

$$R_6 = \frac{\left[SO_4^{2-} \right]}{\left[SO_4^{2-} \right] + K_{SO_4^{2-}}} \frac{K_{FeOOH}}{[FeOOH] + K_{FeOOH}} \frac{K_{O_2}}{[O_2] + K_{O_2}} R_{min}^{s}$$

$$R_7 = \varphi k_{H_2S\text{-}Ox} [O_2] \left[HS^- \right]$$

$$R_8 = \varphi k_{Fe\text{-}Ox} \left[Fe^{2+} \right] [O_2]$$

$$R_9 = (1 - \varphi) k_{FeOOH\text{-}H_2S} [FeOOH] \left[HS^- \right]$$

$$R_{10} = \varphi k_{FeS.form} \left[Fe^{2+} \right] \left[HS^- \right]$$

$$R_{11} = (1 - \varphi) k_{FeS\text{-}Ox} [FeS] [O_2]$$

$$R_{12} = (1 - \varphi) k_{FeS_2.form} [FeS] \left[HS^- \right]$$

$$R_{13} = (1 - \varphi) k_{FeS_2\text{-}Ox} [FeS_2] [O_2]$$

concentrations, as measured by a total Fe extraction at the conclusion of the experiment.

2.5 Numerical model solution

A numerical solution procedure was implemented in the open-source programming language R as fully detailed in Soetaert and Meysman (2012). A reactive transport model essentially consists of one partial differential equation (PDE) for each compound. Together with the mass action laws of the acid-base equilibria, these PDEs form a differential-algebraic system, which was solved using an operator splitting approach (Solution method, 3b, as explained in Hofmann et al., 2008). Following the method-of-lines, the R-package ReacTran uses a finite difference scheme to expand the spatial derivatives of the PDEs over the sediment grid. This grid was obtained by dividing the sediment domain (thickness $L = 5$ cm, the approximate depth of the sediment cores in the incubation experiment) into a uniform grid of 100 sediment layers. After finite differencing, the resulting set of ODEs was integrated using the stiff equation solver vode from the R-package deSolve.

At each time step, the operator splitting approach of the pH model required an additional pH equilibration step. To this end, the numerical integration of the ODE system provided the values of the reaction invariants (TA, SumCO2, SumH2S, SumBOH3) at each future time step. Subsequently, the nonlinear system of algebraic acid-base expressions was

solved for the unknown proton concentration using the iterative method of Follows et al. (2006). Using this proton concentration (or equally pH value), the full speciation could be calculated of all chemical species involved in the acid-base dissociation reactions. The resulting concentrations of the equilibrium species could then be employed in kinetic rate expressions (specifically, the pore water CO_2 concentration was needed in the rate expression for the air-sea gas transfer of CO_2). Further details on this pH model procedure are given by Hofmann et al. (2008).

2.6 Description of model runs

The model was set up to simulate the tidal cycles imposed in the laboratory core incubation experiments, which were exposed and inundated alternately every 6 h.

The model simulations provide flux estimates at each point in time. The fluxes of TA and DIC during inundation and CO_2 fluxes during exposure are reported as the mean over the 6-h exposure/inundation period. These reported mean values include transient ($\sim$ 30 min) spikes in DIC and TA immediately after inundation. The simulation extended over 120 days (i.e., 240 tidal cycles), with a pulse of organic matter added on day 70, simulating the addition of the organic matter source in the laboratory experiments. Table 3 lists an overview of parameters values used in model simulations. These were determined from measured properties, literature values or calibrated to the available dataset. All parameter values were kept constant during the whole simulation period (apart from the organic matter input).

2.7 Sensitivity model runs

The sensitivity of CO_2 flux to the piston velocity was investigated using simulations, where the piston velocity was varied from 0.05 to 5 cm h^{-1}. In each simulation, the initial FeOOH concentration was 19 µmol Fe g^{-1} dry sediment. For each value of the piston velocity, the average flux of CO_2 during exposure was calculated over the complete simulation period (30 tidal cycles). This procedure was repeated for three different initial values of organic matter concentration (2500, 1000 and 600 µmol C g^{-1} dry sediment for the slow-decaying fraction, and 5, 2.5 and 1.3 µmol C g^{-1} dry sediment for the fast-decaying fraction, respectively), to investigate the sensitivity of CO_2 flux to the piston velocity under different amounts of organic matter loading.

The availability of reactive oxidised iron (FeOOH) controls alkalinity production in the sediment and, hence, we performed a second series of simulations to investigate the sensitivity of the model towards the initial sedimentary FeOOH concentration. To determine the effect of FeOOH availability on TA production, simulations were run with a fixed initial concentration of CH2O ($\sim$ 2500 µmol CH$_2$O g^{-1} dry sediment), but with various FeOOH concentrations (7.6, 19 and 95 µmol Fe g^{-1} dry sediment). The values of 19 and

Table 3. Overview of model parameter values.

Constant	Value	Units
Porosity	0.8	–
rho.sed (density of solid sediment)	2.6	$g\,cm^{-3}$
Piston velocity	1	$cm\,h^{-1}$
K.fast (highly labile organic matter)	25	yr^{-1}
K.slow (less labile organic matter)	0.6	yr^{-1}
K_O$_2$ (Monod constant for O$_2$ consumption)	0.005	$\mu mol\,cm^{-3}$
K_FeOOH (Monod constant for FeOOH reduction)	200*rho.sed	$\mu mol\,cm^{-3}$
K_SO$_4^{2-}$ (Monod constant for SO$_4^{2-}$ reduction)	1.6	$\mu mol\,cm^{-3}$
k_H$_2$S.Ox (Kinetic constant for H$_2$S oxidation)	1.6×10^7	$\mu mol^{-1}\,cm^3\,yr^{-1}$
k_Fe.Ox (Kinetic constant for Fe oxidation)	2.0×10^4	$\mu mol^{-1}\,cm^3\,yr^{-1}$
k_FeS.Ox (Kinetic constant for FeS oxidation)	160	$\mu mol^{-1}\,cm^3\,yr^{-1}$
k_FeS$_2$.Ox (Kinetic constant for FeS$_2$ oxidation)	0	$\mu mol^{-1}\,cm^3\,yr^{-1}$
k_Fe.H$_2$S (Kinetic constant for FeOOH/H$_2$S redox reaction)	2.57	$\mu mol^{-1}\,cm^3\,yr^{-1}$
k_FeS.form (Kinetic constant for FeS formation)	1×10^8	$\mu mol^{-1}\,cm^3\,yr^{-1}$
k_FeS$_2$.form (Kinetic constant for FeS$_2$ formation)	1	$\mu mol^{-1}\,cm^3\,yr^{-1}$

95 μmol Fe g^{-1} dry sediment are the low and high estimates of sediment FeOOH concentrations in the core experiment sediment, respectively. The value of 7.6 μmol Fe g^{-1} dry sediment was chosen as a low value for a comparison with our estimates.

3 Results

3.1 Experimental

There was little variation in the DIC fluxes over the entire course of the experiment in the $-$OM treatment with a mean value of 1.3 mmol m^{-2} h^{-1} over the 120 days (Fig. 2). In the $+$OM treatment, DIC fluxes were the same as the $-$OM treatment within experimental uncertainty in the first 70 days of the experiment before the organic matter was added (Fig. 2). After the organic matter addition, DIC fluxes substantially increased to a maximum of $\sim$ 5.0 mmol m^{-2} h^{-1}, and then decreased again to $\sim$ 2.0 mmol m^{-2} h^{-1} over a time period of 40 days after organic matter addition. Alkalinity fluxes were initially high in both $-$OM and $+$OM treatments, steadily decreasing from $>$ 1.4 mmol m^{-2} h^{-1} at the start of the experiment to attain a negligible alkalinity flux after 60 days. The most likely explanation for this observation is that there
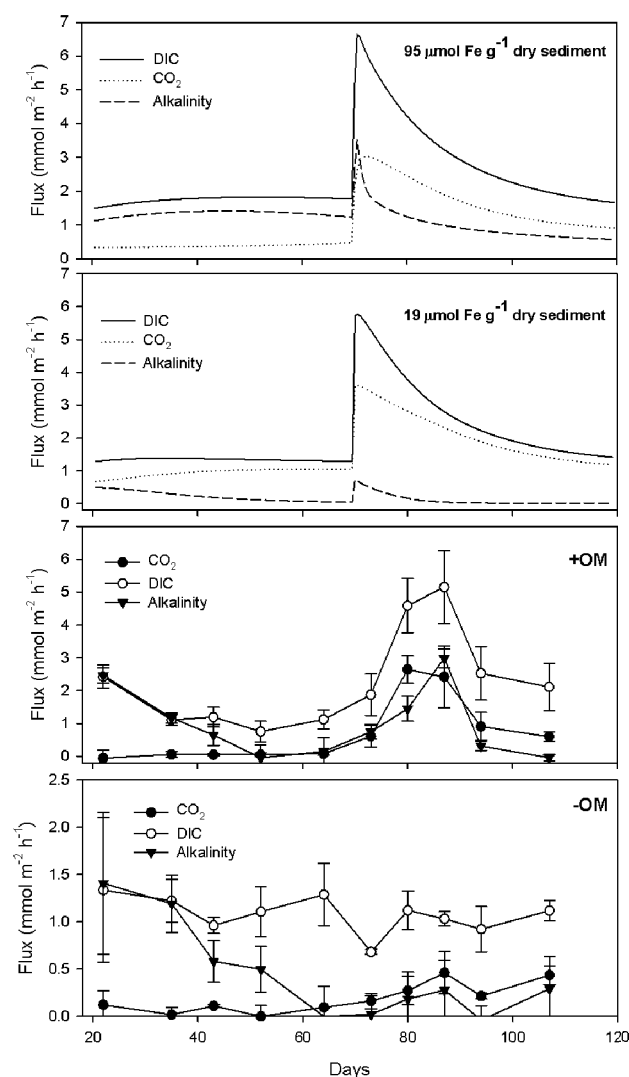

Fig. 2. Simulated mean fluxes of CO$_2$ during exposure (CO$_2$), dissolved inorganic carbon (DIC) and alkalinity during inundation in the computer simulation with 95 and 19 μmol Fe g^{-1} sediment (d/w) and laboratory core incubation fluxes with ($+$OM) and without ($-$OM) added organic matter. Error bars are standard deviations across 10 replicates.

was build-up of iron sulfides, whose rate of formation slowed over time. We hypothesise that initially, a large pool of Fe(III) was formed during sediment pre-treatment, which was subsequently reduced to metal sulfides. Dissimilatory iron reduction produces alkalinity (TA : DIC = 8, see R9 in Table 2), but as the pool of Fe(III) is depleted, alkalinity production will decrease over time. After the pulsed addition of organic matter, alkalinity fluxes increased rapidly to a maximum of 3.0 mmol m^{-2} h^{-1} before decreasing again rapidly. The CO$_2$ fluxes during exposure were initially very low in both treatments ($\sim$ 0.10 mmol m^{-2} h^{-1}). In the $-$OM treatment, the CO$_2$ flux increased after 60 days, coinciding with

the decrease and cessation of alkalinity fluxes (fluxes not significantly different from zero, shown by the error bars). In the +OM treatment, there was an increase in CO_2 fluxes after the addition of organic matter, reaching a maximum of ~ 2.5 mmol m^{-2} h^{-1}. The CO_2 fluxes decreased again to ~ 0.60 mmol m^{-2} h^{-1} at the conclusion of the experiment.

3.2 Model simulations

To match with the laboratory experiments, the data from the model were truncated before 20 days (Fig. 2). From day 20 to 70, the simulation yielded inundated DIC fluxes between ~ 1.2 and ~ 1.4 mmol m^{-2} h^{-1}. Immediately after the OM addition at day 70, the DIC flux increased to a maximum of ~ 5.7 mmol m^{-2} h^{-1}. The TA flux decreased from ~ 0.48 to ~ 0.40 mmol m^{-2} h^{-1} before the OM addition, then increased to a maximum of ~ 0.74 mmol m^{-2} h^{-1} after the addition. The CO_2 flux during exposure was between ~ 0.66 and ~ 1.0 mmol m^{-2} h^{-1} before the OM addition, and rose to a maximum of ~ 3.6 mmol m^{-2} h^{-1} after the addition of the OM, then decreasing again to ~ 1.2 mmol m^{-2} h^{-1} by the end of the simulation. The peak flux during the simulation is shifted forward in time relative to the core incubations indicating a delayed response of organic matter mineralisation under experimental conditions. This is expected, as the bacterial community first needs to grow to consume the bioavailable organic matter. In the computer simulation, no lag phase occurs, as the model formulation does not include population growth and, thus, assumes an instantaneous response of microbial metabolism.

In the model simulations, DIC fluxes were consistently higher during inundation than CO_2 fluxes during the corresponding exposure periods (Fig. 3). The discrepancy between DIC and gaseous CO_2 fluxes appears to increase with increasing respiration, shown by the divergence of the simulation data from the 1 : 1 line as DIC flux increases. This pattern was very similar to that previously observed for intact sediments collected from tidal flats (Cook et al., 2004) (Fig. 3).

The fluxes of gaseous CO_2 during exposure and the fluxes of DIC and TA during exposure were highly sensitive to initial Fe concentrations in the sediment. This can be evaluated by calculating the mean fluxes over the period before the organic matter pulse (Fig. 4). The high Fe concentration resulted in a lower CO_2 flux during exposure (~ 0.65 vs. ~ 0.35 mmol m^{-2} h^{-1} for the 19 and 95 µmol Fe g^{-1} dry sediment). There was also a large discrepancy between alkalinity fluxes, where the high Fe concentration resulted in a higher TA flux (0.80 mmol m^{-2} h^{-1} versus 1.4 mmol m^{-2} h^{-1} for the 19 and 95 µmol Fe g^{-1} dry sediment simulations). The difference between DIC fluxes were smaller, with a flux of ~ 1.8 mmol m^{-2} h^{-1} for the simulation with 95 µmol Fe g^{-1} dry sediment and ~ 1.6 mmol m^{-2} h^{-1} for the simulation with 19 µmol Fe g^{-1} dry sediment.
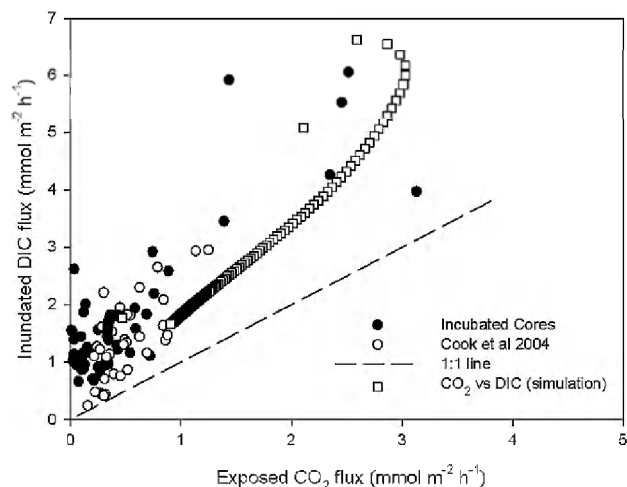

Fig. 3. Fluxes of dissolved inorganic carbon (DIC) versus exposed CO_2 fluxes for two experimental datasets and a model simulation. Incubated core experiments represent both the + and −OM treatments.

3.3 Simulation profiles

The profile of FeOOH in the top 0.5 cm of sediment changed dramatically upon the addition of the organic matter pulse to the top 0.2 cm (Fig. 5). The profile taken two tidal cycles before the pulse shows the FeOOH reaching ~ 15 µmol Fe g^{-1} dry sediment in the surface layer and decreasing with increasing depth. One tidal cycle after the addition of organic matter, FeOOH has begun to oxidise, with the concentration in the top 0.2 cm falling to a maximum of 2 µmol Fe g^{-1} dry sediment in the surface layer. Below 0.2 cm, the FeOOH profile is similar between the two times, as the organic matter concentration has not changed in this domain.

4 Discussion

4.1 Alkalinity producing reactions

The production of alkalinity can be attributed to several key processes; ammonia release, net denitrification, net sulfate reduction and to a lesser extent, dissolved organic carbon release (Hammond et al., 1999). Berner et al. (1970) proposed the idea of sulfate reduction as an alkalinity producing process. It was noted that sulfate reduction coupled with the precipitation of the stable iron sulfides FeS and FeS$_2$ produces one mole of alkalinity per mole of carbon mineralised (Berner et al., 1970) (Eq. 1).

$$6CH_2O + 3SO_4^{2-} + 2FeOOH \rightarrow FeS + FeS_2 + 6HCO_3^- + 4H_2O \quad (1)$$

In this representation of sulfate reduction, the supply of Fe(III) to the sediment enables the burial of reduced sulfur compounds as iron sulfides (FeS) or pyrite (FeS$_2$). This burial of reduced sulfur prevents sulfide oxidation and,
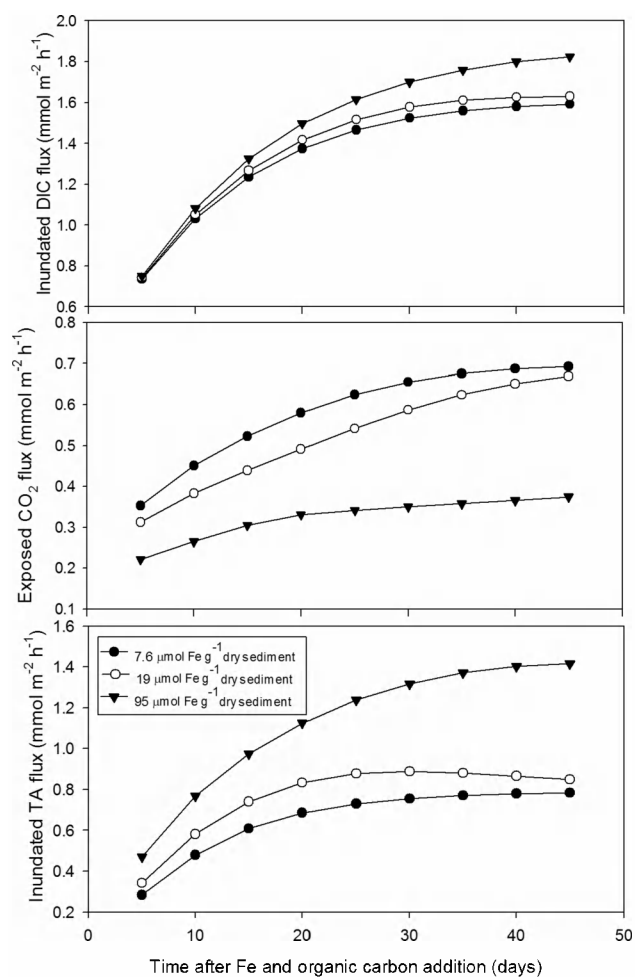
Fig. 4. Fluxes of dissolved inorganic carbon (DIC), exposed CO_2 and alkalinity fluxes for a simulation of a 50 day period with an imposed profile of 7.6, 19 and 95 $\mu mol\,g^{-1}$ sediment (d/w) FeOOH.

Fig. 5. A simulation showing the FeOOH concentration before and after an organic matter pulse with initial FeOOH concentration of 19 $\mu mol\,g^{-1}$ sediment (d/w). Note: The step around 0.2 cm is due to the pulse of organic matter added to only the top 0.2 cm.

hence, it prevents the alkalinity generated by sulfate reduction being consumed again (Eq. 2).

$$HS^- + 2O_2 \rightarrow SO_4^{2-} + H^+ \qquad (2)$$
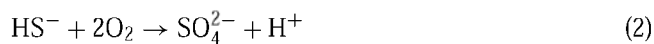
Upon exposure to oxygen, iron sulfides can also oxidise, leading to alkalinity consumption (and, hence, no net alkalinity generation by sulfate reduction) (Eq. 3).

$$FeS + 2.25O_2 + 2.5H_2OFe(OH)_3 + SO_4^{2-} + 2H^+ \qquad (3)$$
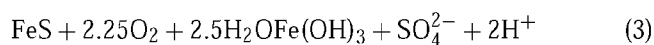
However, the rate of this reaction is typically lower than that of free sulfide oxidation (see Table 3). More importantly, one requires a suitable transport process, that either moves the reduced sulfur compounds upwards to the oxic zone (like bioturbation), or transfers oxygen down into anoxic layers (like bio-irrigation). In the experimental setup here, such transport processes are not present.

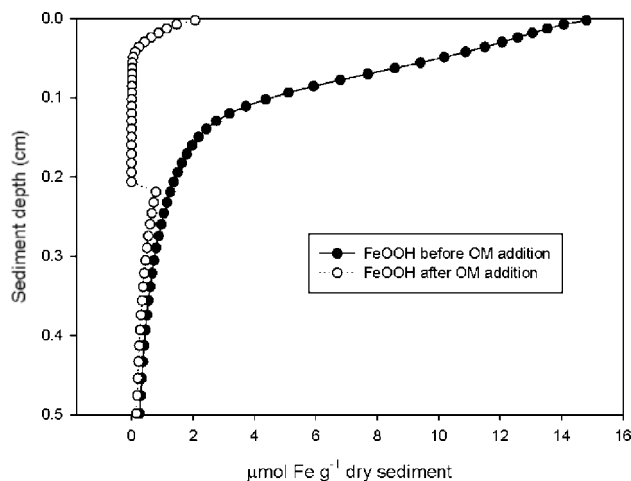Hu and Cai (2011) reviewed the factors controlling alkalinity generation in ocean margins in sediment and concluded that the burial of pyrite and the denitrification of NO_3^- derived from the continents were the only net sources of alkalinity in ocean margin sediments. As the cycling of sulfur is closely linked with that of iron, we included both sulfur and iron geochemistry in the diagenetic model. In our experiments, denitrification was unlikely to be a significant source of alkalinity generation because of the lack of NO_3^- in the overlying water of our incubations. Coupled nitrification denitrification will not results in significant net alkalinity generation (Hu and Cai, 2011). Consequently, we did not model the effect of denitrification on alkalinity in this model. Dissolved organic matter and HPO_4^{2-} have been shown to contribute to alkalinity fluxes (Cai et al., 2010), but reactions involving sulfur (and it interactions with iron) are the major processes controlling the alkalinity balance within the sediment and, hence, only these processes are considered. We are confident that the model used here represents the critical anaerobic alkalinity-generating processes that are important in our experimental set up.

4.2 Model sensitivity towards piston velocity

At piston velocities $> 1\,cm\,h^{-1}$ the CO_2 efflux reached a stable value and this asymptotic CO_2 efflux increased proportionally with initial organic matter content (or total mineralisation) (Fig. 6). Decreasing the piston velocity below $0.5\,cm\,h^{-1}$ reduced CO_2 fluxes during sediment exposure. This can be attributed to the slower efflux of CO_2 for a given CO_2 concentration gradient (transport control), and a slower flux of O_2 into the sediment resulting in less aerobic respiration. Indeed, we found the rate of aerobic respiration to decrease with decreasing piston velocity (data not shown). Initially we thought that the alkalinity flux would remain
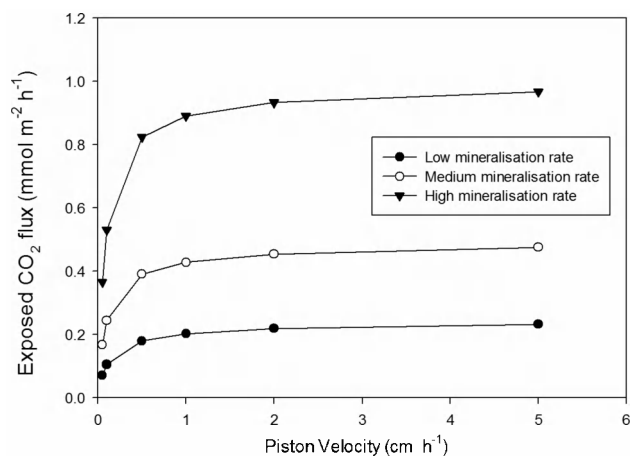
Fig. 6. Exposed flux of CO_2 with varying piston velocity and respiration rate. Low, medium and high mineralisation rates refer to peak DIC productions of approx. 600, 1300 and 2600 μmol m^{-2} h^{-1}, respectively.

constant upon changing piston velocity. It was noted, however, that there was an increase in alkalinity production by 7 % as the piston velocity was decreased from 5 to 0.05 (data not shown) indicating that anaerobic respiration accounted for a greater proportion of the total respiration. Higher respiration rates were more sensitive to decreasing piston velocities. We concluded that when the piston velocity is greater than 1 cm h^{-1}, exchange will be limited by production of CO_2 (reaction control), rather than transport across the air-water interface (Fig. 6). For the remainder of the simulations, the piston velocity was fixed at 1 cm h^{-1}, the lowest of values found by various researchers across the water-air interface in estuarine and riverine systems, as summarised by Raymond et al. (2000).

4.3 Agreement of simulations with experimental data

There was a general agreement between experimental flux data and the model simulations. Both model and experimental data showed that DIC fluxes from the sediment during tidal inundation are higher than CO_2 fluxes during exposure. This difference was most pronounced at the start of the experiment and after the addition of organic matter. At the start of the experiments there was a rapid alkalinity generation which can be explained by the formation of FeS as the Fe(III) initially present within the surface sediment was reduced. After the pulse of organic matter, the oxygen penetration in the sediment is reduced and a higher rate of anaerobic carbon mineralisation takes place. This leads then to increased rates of reduced sulfur production, FeS burial and net alkalinity production. The reduction of Fe in the surface of the sediment leads to a transient alkalinity flux and associated increase in the discrepancy between gaseous CO_2 flux and DIC flux (Fig. 5). This observation is seen in both the model and the

laboratory incubations, although there is a slight offset due to the fact that there is a delay in the maximum respiration rate in the laboratory incubations compared to the model.

In our simulations, reduced sulfur production continues after FeOOH is exhausted, but it is reoxidised as free sulfide diffuses upwards into the oxygenated surface layers of sediment. Nonetheless, a relatively small alkalinity flux still leaves the sediment, as there is some build up of H_2S in the sediment pore waters (The diffusion of sulfide into the oxic layer, and its subsequent oxidation is slower than its production within the deeper layers of the sediment).

The dynamics of this simulation/experiment have strong environmental relevance being representative of a resuspension event or the deposition of fresh sediment from the catchment and the deposition of organic matter. This highlights the importance of environmental dynamics in controlling the relative loss of CO_2 and DIC from intertidal sediment. Indeed, in coastal sediments, periodically high fluxes of alkalinity are observed following periods of high organic matter input (Ferguson et al., 2003a). Hargrave and Phillips (1981) note the significance of short-term organic matter deposition, with high supply rates, relative to mineralisation rates, causing a burial of organic matter in deeper, anoxic layers of the sediment.

4.4 Model sensitivity towards sedimentary iron

The sensitivity of the model (Fig. 7) to solid-phase iron (Fe) suggests that the delivery of fresh (oxidised) Fe controls how much mineralised carbon is exported to the atmosphere (as CO_2) versus the ocean (as alkalinity). In the simulation, a large input of Fe leads to a higher rate of alkalinity production through FeS$_2$ burial (FeOOH consumption), and a corresponding lower CO_2 efflux during exposure (Fig. 4). The sensitivity of the model to Fe agrees with the literature (Hu and Cai, 2011; Berner et al., 1970), which suggests that FeS$_2$ burial is the most important process controlling alkalinity production. The present work shows that in high carbon systems such as intertidal sediments, Fe will be the limiting species in pyrite burial, despite the role of carbon as the mediating species in pyrite burial globally (Hu and Cai, 2011).

The temporal change of TA fluxes also differs considerably. TA flux stabilises after 30 days in the simulations with the lower Fe concentrations, whereas at higher Fe concentrations, TA flux continues to increase. This is due to the reduction of all the oxidised Fe, creating a higher net production of alkalinity. For simulations with little or no Fe, there is a higher temporary sink of HS$^-$ in the sediment pore waters during intense alkalinity production (Fig. 7) as insoluble iron sulfides cannot form. Subsequent alkalinity consumption occurs as the HS$^-$ is reoxidised. The effect of the reoxidation of reduced sulfur can be seen in Fig. 7, which shows the simulation with no FeOOH having lower pH and, thus, higher CO_2 concentration, than the simulation with 95 μmol Fe g^{-1} dry sediment. The alkalinity concentration (as indicated by
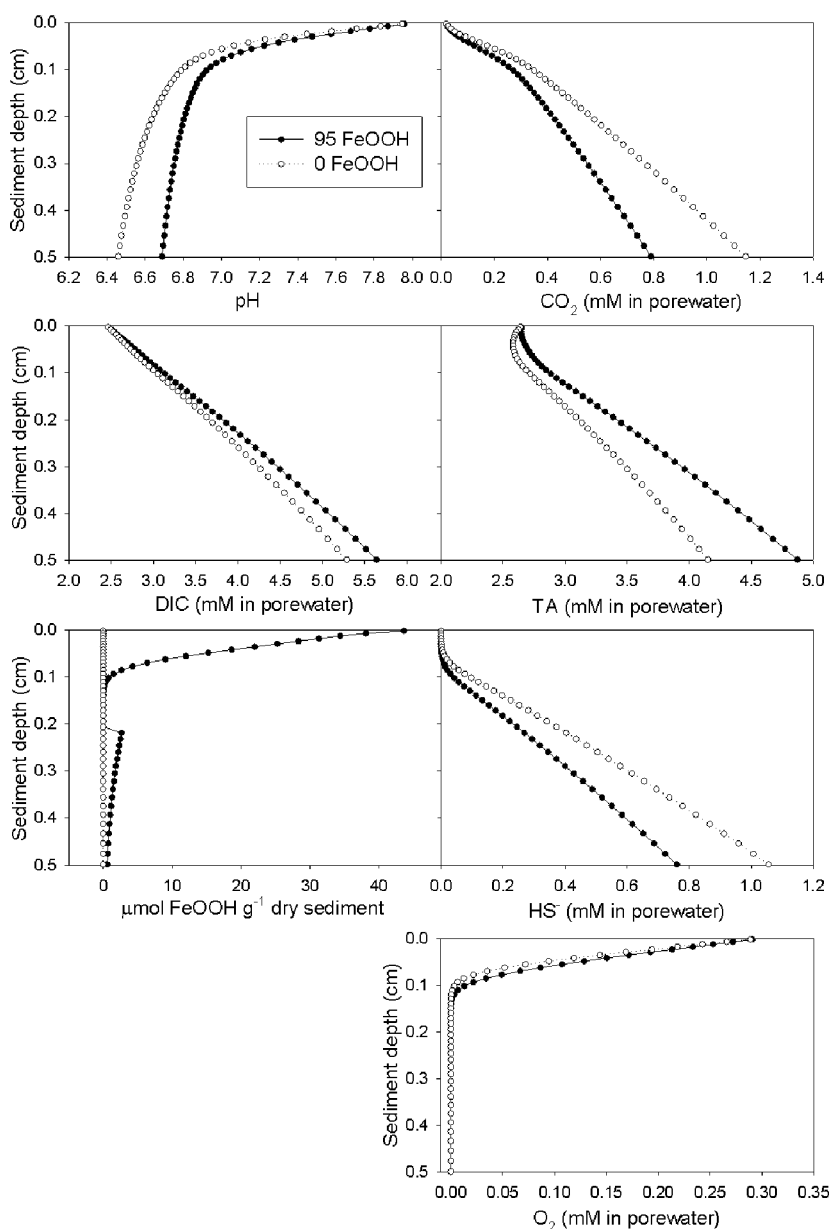
Fig. 7. Profiles of pH, CO_2, DIC, TA, FeOOH and HS^- and O_2 from two simulations. Empty circles represent a simulation with no FeOOH, whereas filled circles represent 95 μmol g^{-1} sediment (d/w) FeOOH.

HCO_3^- and CO_3^{2-}) throughout the FeOOH containing profile is also considerably higher. During periods where respiration is extremely high, HS^- has the potential to by-pass the small oxic zone in the sediment and so the HS^- can reach the water column before it is reoxidised. In this situation, the numeric simulation will show a net alkalinity flux from the sediment. In reality, immediate reoxidation of HS^- in the overlying water column will directly consume this alkalinity.

With regard to carbon budgets, the effect of anaerobic carbon metabolism is important as higher alkalinity export to the ocean creates a higher CO_2 buffering capacity for the up-

take of atmospheric CO_2. The effect of anaerobic alkalinity production on atmospheric carbon uptake in coastal seas has been estimated at up to 60 % of the total uptake (Thomas et al., 2009). This is an upper estimate, as it neglects alkalinity consumed during nitrification (Hu and Cai, 2011). In regions with high anthropogenic disturbance, large amounts of terrestrial carbon is exported towards coastal oceans (Frankignoulle et al., 1996, 1998; Abril et al., 2002). Increased organic carbon loading in estuaries due to anthropogenic land use represents an anthropogenic carbon source to the atmosphere upon its breakdown. More anthropogenically

disturbed catchments will also export more sediment and, hence, more Fe(III) (Asselman et al., 2003; Walling, 1999) to estuaries, which may partially offset larger CO_2 emissions from increased labile organic carbon export to estuaries. The significance of this offset remains to be investigated.

5 Conclusions

The laboratory data and field data (Cook et al., 2004) and computer simulations clearly show that gaseous CO_2 fluxes during exposure on tidal flats are likely to under-estimate total carbon mineralisation. This finding has clear implications for research in this field, given that total inorganic carbon fluxes for intertidal sediments have generally been estimated using only gaseous CO_2 fluxes on the exposed sediments (Migné et al., 2005; Middelburg et al., 1996). The results of this study demonstrate the importance of considering both exposed and inundated fluxes in studies of intertidal metabolism, which may be quite different, depending on the extent to which there is a net accumulation of reduced solutes.

References

Abril, G., Nogueira, M., Etcheber, H., Cabecadas, G., Lemaire, E., and Brogueira, M.: Behaviour of organic carbon in nine contrasting european estuaries, Estuarine, Coast. Shelf Sci., 54, 241–262, 2002.

Almgren, T., Dyrssen, D., and Fonselius, S.: Determination of alkalinity and total carbonate, in: Methods of seawater analysis, edited by: Grasshoff, K., Ehrhardt, M., and Kremling, K., Springer-Verlag, Chemie, Weinheim, 99–123, 1983.

Alongi, D., Tirendi, F., Dixon, P., Trott, L., and Brunskill, G.: Mineralization of organic matter in intertidal sediments of a tropical semi-enclosed delta, Estuar. Coast. Shelf S., 48, 451–467, 1999.

Asselman, N. E. M., Middelkoop, H., and Van Dijk, P. M.: The impact of changes in climate and land use on soil erosion, transport and deposition of suspended sediment in the river rhine, Hydrol. Process., 17, 3225–3244, 2003.

Berner, R. A., Scott, M. R., and Thomlinson, C.: Carbonate alkalinity in the pore waters of anoxic marine sediments, Limnol. Oceanogr., 15, 544–549, 1970.

Boudreau, B. P.: The diffusive tortuosity of fine-grained unlithified sediments, Geochim. Cosmochim. Ac., 60, 3139–3142, 1996.

Boudreau, B. P.: Diagenetic models and their implementation: Modelling transport and reactions in aquatic sediments, Springer, Berlin and New York, 1997.

Brotas, V., Amorim-Ferreira, A., Vale, C., and Catarino, F.: Oxygen profiles in intertidal sediments of ria formosa (s. Portugal), Hydrobiologia, 207, 123–130, 1990.

Cai, W., Pomeroy, L., Moran, M., and Wang, Y.: Oxygen and carbon dioxide mass balance for the estuarine-intertidal marsh complex of five rivers in the southeastern us, Limnol. Oceanogr., 44, 639–649, 1999.

Cai, W. J., Luther, G. W., Cornwell, J. C., and Giblin, A. E.: Carbon cycling and the coupling between proton and electron transfer reactions in aquatic sediments in lake champlain, Aquat. Geochem., 16, 421–446, 2010.

Cook, P., Butler, E., and Eyre, B.: Carbon and nitrogen cycling on intertidal mudflats of a temperate australian estuary i. Benthic metabolism, Mar. Ecol.-Prog. Ser., 280, 25–38, 2004.

Ferguson, A. J. P., Eyre, B. D., and Gay, J. M.: Organic matter and benthic metabolism in euphotic sediments along shallow subtropical estuaries, northern new south wales, australia, Aquat. Microb. Ecol., 33, 137–154, 2003.

Follows, M. J., Ito, T., and Dutkiewicz, S.: On the solution of the carbonate chemistry system in ocean biogeochemistry models, Ocean Model., 12, 290–301, 2006.

Frankignoulle, M., Bourge, I., and Wollast, R.: Atmospheric co_2 fluxes in a highly polluted estuary (the scheldt), Limnol. Oceanogr., 41, 365–369, 1996.

Frankignoulle, M., Abril, G., Borges, A., Bourge, I., Canon, C., Delille, B., Libert, E., and Théate, J.: Carbon dioxide emission from european estuaries, Science, 282, 434–436, 1998.

Gribsholt, B. and Kristensen, E.: Benthic metabolism and sulfur cycling along an inundation gradient in a tidal spartina anglica salt marsh, Limnol. Oceanogr., 48, 2151–2162, 2003.

Hammond, D., Giordani, P., Berelson, W., and Poletti, R.: Diagenesis of carbon and nutrients and benthic exchange in sediments of the northern adriatic sea, Mar. Chem., 66, 53–79, 1999.

Hargrave, B. and Phillips, G.: Annual in situ carbon dioxide and oxygen flux across a subtidal marine sediment, Estuar. Coast. Shelf S., 12, 725–737, 1981.

Hofmann, A. F., Meysman, F. J. R., Soetaert, K., and Middelburg, J. J.: A step-by-step procedure for pH model construction in aquatic systems, Biogeosciences, 5, 227–251, doi:10.5194/bg-5-227-2008, 2008.

Hofmann, A. F., Soetaert, K., Middelburg, J. J., and Meysman, F. J. R.: Aquaenv: An aquatic acid–base modelling environment in r, Aquat. Geochem., 16, 507–546, 2010.

Hu, X. and Cai, W. J.: An assessment of ocean margin anaerobic processes on oceanic alkalinity budget, Global Biogeochem. Cy., 25, 1–11, 2011.

Joye, S. B., de Beer, D., Cook, P. L. M., and Perillo, G.: Biogeochemical dynamics of coastal tidal flats, in: Coastal wetlands: an integrated ecosystem approach, edited by: Perillo, G., Cahoon, D., and Brinson, M., Elsevier, Amsterdam, The Netherlands, 345–374, 2009.

Kristensen, E.: Benthic fauna and biogeochemical processes in marine sediments: Microbial activities and fluxes, in: Nitrogen cycling in coastal marine environments, edited by: Blackburn, T. H. and Sorensen, J., John Wiley and Sons, Chichester, 275–299, 1988.

Lord, C. J.: A selective and precise method for pyrite determination in sedimentary materials, J. Sediment. Res., 52, 664–666, 1982.

Meysman, F. J. R., Middelburg, J. J., Herman, P. M. J., and Heip, C. H. R.: Reactive transport in surface sediments, II. Media: An object-oriented problem-solving environment for early diagenesis, Comput. Geosci., 29, 301–318, 2003.

Middelburg, J., Klaver, G., Nieuwenhuize, J., Wielemaker, A., De Haas, W., Vlug, T., and Van der Nat, J.: Organic matter mineralization in intertidal sediments along an estuarine gradient, Mar. Ecol.-Prog. Ser., 132, 157–168, 1996.

Migné, A., Davoult, D., Bourrand, J. J., and Boucher, G.: Benthic primary production, respiration and remineralisation: In situ measurements in the soft-bottom abra alba community of the western english channel (north brittany), J. Sea Res., 53, 223–229, 2005.

Raymond, P., Bauer, J., and Cole, J.: Atmospheric co_2 evasion, dissolved inorganic carbon production, and net heterotrophy in the york river estuary, Limnol. Oceanogr., 45, 1707–1717, 2000.

Roy, R., Roy, L., Vogel, K., Porter-Moore, C., Pearson, T., Good, C., Millero, F., and Campbell, D.: The dissociation constants of carbonic acid in seawater at salinities 5 to 45 and temperatures 0 to 45 °C, Mar. Chem., 44, 249–267, 1993.

Satienperakul, S., Cardwell, T. J., Cattrall, R. W., McKelvie, I. D., Taylor, D. M., and Kolev, S. D.: Determination of carbon dioxide in gaseous samples by gas diffusion-flow injection, Talanta, 62, 631–636, 2004.

Soetaert, K. and Meysman, F.: Reactive transport in aquatic ecosystems: Rapid model prototyping in the open source software r, Environ. Model. Softw., 32, 49–60, 2012.

Soetaert, K., Petzoldt, T., and Meysman, F. J. R.: Marelac: Tools for aquatic sciences, R package version 2.1.1., 2010.

Thomas, H., Schiettecatte, L.-S., Suykens, K., Koné, Y. J. M., Shadwick, E. H., Prowe, A. E. F., Bozec, Y., de Baar, H. J. W., and Borges, A. V.: Enhanced ocean carbon storage from anaerobic alkalinity generation in coastal sediments, Biogeosciences, 6, 267–274, doi:10.5194/bg-6-267-2009, 2009.

Walling, D.: Linking land use, erosion and sediment yields in river basins, Hydrobiologia, 410, 223–240, 1999.

Westrich, J. T. and Berner, R. A.: The role of sedimentary organic matter in bacterial sulfate reduction: The g model tested, Limnol. Oceanogr., 29, 236–249, 1984.